Article

Thermodynamically spontaneously intercalated H_3O^+ enables LiMn$_2$O$_4$ with enhanced proton tolerance in aqueous batteries

Jiangfeng Huang[1,4], Liang Xue ✉[1,4] ✉, Yin Huang[1], Yanchen Jiang[1], Ping Wu[2], Xiulin Fan ✉[3] & Junwu Zhu ✉[1] ✉

LiMn$_2$O$_4$ (LMO) is an attractive positive electrode material for aqueous lithium-ion batteries (ALIBs), but its inferior cycle performance limits the practical application. The degradation mechanism of LMO in ALIBs is still unclear, resulting in inability to predictably improve its structural stability. The electrode/electrolyte interface is believed to play an important role in electrode degradation. However, the interactions of the water-containing electrode/electrolyte interface of LMO are underexplored. In this work, we demonstrate the insertion of H_3O^+ into LMO during cycling in aqueous electrolyte and elucidate the paradoxical effects of H_3O^+. The crystal H_3O^+ enhances the structural stability of LMO by forming a gradient Mn^{4+}-rich protective shell, but an excess amount of crystal H_3O^+ leads to poor Li^+ conductivity, resulting in rapid capacity fading. Combining electrochemical analyses, structural characterizations, and first-principles calculations, we reveal the intercalation of H_3O^+ into LMO and its associated mechanism on the structural evolution of LMO. Furthermore, we regulate the crystal H_3O^+ content in LMO by modifying the hydrogen bond networks of aqueous electrolyte to restrict H_2O molecule activity. This approach utilizes an appropriate amount of crystal H_3O^+ to enhance the structural stability of LMO while maintaining sufficient Li^+ diffusion.

Electricity generation from sustainable energies pursues safe, economical, and long-life secondary batteries. Aqueous rechargeable batteries are promising power sources for large-scale energy storage systems[1-3]. Compared with lead-acid, nickel-metal hydride, nickel-chromium, etc., aqueous lithium-ion batteries (ALIBs) using Li^+ intercalation should have higher energy density, higher rate performance, and longer cycle life[4,5]. Nevertheless, the metal oxide electrode materials for ALIBs usually suffer from protonation, metal dissolution, and structural degradation in aqueous electrolytes, resulting in rapid capacity fading[6-9].

Among them, spinel-type LiMn$_2$O$_4$ (LMO) has high thermodynamic structural stability relative to layered-type metal oxide materials and has satisfactory specific capacity in aqueous electrolytes[10-12]. Unfortunately, the cycle stability of LMO in aqueous electrolytes is still far from commercial application[13,14]. At present, the

[1]Key Laboratory for Soft Chemistry and Functional Materials, Ministry of Education, School of Chemistry and Chemical Engineering, Nanjing University of Science and Technology, Nanjing, China. [2]Jiangsu Key Laboratory of New Power Batteries, School of Chemistry and Materials Science, Nanjing Normal University, Nanjing, China. [3]State Key Laboratory of Silicon and Advanced Semiconductor Materials, School of Materials Science and Engineering, Zhejiang University, Hangzhou, China. [4]These authors contributed equally: Jiangfeng Huang, Liang Xue. ✉e-mail: xueliang@njust.edu.cn; zhujw@njust.edu.cn

reasons for the performance degradation of LMO in ALIBs are unclear, and no rules can be drawn from the current research results. It's widely acknowledged that the proton triggers Mn dissolution and severe structural degradation, resulting in poor cycling stability[10,15,16]. It can be speculated that in aqueous electrolytes, where the H^+ quantity is higher than in organic electrolytes, the kinetics of Mn dissolution and structural degradation should be accelerated. However, based on recent studies, LMO shows puzzling cycle performance in various aqueous electrolytes. For instance, Li et al.[17] reported that the LMO with exposed (111) crystal facets has a capacity retention of 87% after 200 cycles in 2.5 M Li_2SO_4. The full cell $LiMn_2O_4 || Li_4Ti_5O_{12}$ which is based on eutectic electrolyte (4.5 m lithium bis(trifluoromethanesulfonyl) imide (LiTFSI)−KOH−CO(NH$_2$)$_2$−H$_2$O) shows the capacity retention of 92% after 470 cycles[18]. Yuan et al.[19] reported that the LMO has a capacity retention of 69.3% after 400 cycles in 2 M Li_2SO_4. We carefully test the cycle performance of the LMO in 1 M Li_2SO_4 aqueous electrolyte and find that the capacity retention of LMO in aqueous electrolytes is superb before 150 cycles, but decayed rapidly in subsequent cycles. These works and our experiments suggest that the interfacial interaction of LMO in aqueous electrolytes is still underexplored.

There are a significant number of H_2O molecules on the surface of electrode particles in aqueous electrolytes. Unlike organic molecules, H_2O molecules have smaller sizes and are more reactive, making them easier to insert into the crystal lattice. In aqueous electrolytes, the electrophilic attack of protons often drives the irreversible transformation of layered materials (e.g., $LiCoO_2$) into electrochemically inert spinel phases[20,21]. On the other hand, it has been reported that the insertion of crystal H_2O (or H_3O^+) into transition metal oxide materials typically enhances specific physical chemistry properties, such as expansion of interlayer distance[22], suppression of layered-to-spinel transitions[23], and improvement in proton tolerance[24], etc. Nevertheless, the intercalation of H_2O (or H_3O^+) into LMO has not been reported, and the effect of interface or lattice H_2O (or H_3O^+) on LMO's charge/discharge process in aqueous electrolytes remains unclear. Thus, the interactions between H_2O (or H_3O^+) and LMO need to be elucidated for further understanding the mechanism of structure evolution of LMO during charge/discharge process in aqueous electrolytes and its correlation with cycle performance.

In this work, we advance the electrochemical reaction mechanism for LMO in aqueous electrolyte. We demonstrate that the insertion of H_3O^+ into LMO lattice during the charge/discharge progress can significantly enhance the structure stability of LMO, but has a detrimental effect on Li^+ diffusion kinetics. In aqueous electrolyte, the trace inserted H_3O^+ enables LMO to perform superior structure stability and better capacity retention than those in organic electrolyte. After further cycling, the H_3O^+ content increases and tends to saturation, at this point, the LMO exhibits sluggish Li^+ diffusion kinetics and shows an accelerated decline in capacity retention. Therefore, the content of H_3O^+ is crucial for structure stability and cycle performance. The revelation of the interaction between LMO and H_3O^+ in aqueous electrolyte provides insight into the understanding of the capacity fading of LMO in aqueous electrolyte and inspires substantial strategies for designing high-performance ALIBs.

Results

Intercalation of H_3O^+ into LMO lattice

The X-ray diffraction (XRD) pattern and scanning electron microscope (SEM) images of the synthesized LMO are shown in Supplementary Figs. 1, 2, respectively. The results indicate that the powdery LMO sample can be well indexed to spinel structure with a space group of $Fd-3m$. For the electrochemical tests of LMO in this work, studies in the aqueous electrolytes (1 M Li_2SO_4 in ultra-pure water with or without additive) are performed in a three-electrode cell (the cell structure is shown in Supplementary Fig. 3a) and studies in organic electrolytes (1 M $LiPF_6$ in EC:DMC = 1:1) are performed in a coin cell (CR2032, the

cell structure is shown in Supplementary Fig. 3b). It is crucial to find a reference electrode with stable potential to study the electrochemical behavior of the working electrode. Unstable voltage plateaus or mismatch of capacity between positive and negative electrodes will cause the charge/discharge curves of the working electrode to deviate from reality, causing the transition of voltage plateaus voltage slope, or leading to the emergence of additional voltage plateaus. Since Li metal has a large theoretical capacity (3860 mAh g^{-1}) and a stable operating voltage plateau, it is commonly used as the negative electrode to provide a consistent voltage reference in organic electrolytes. However, Li metal is sensitive to moist atmosphere. Therefore, we assemble LMO and Li metal negative electrode into well-sealed coin cells to test the electrochemical properties of LMO in an organic electrolyte. For aqueous electrolytes, the drastic reaction between Li metal and H_2O hinders the application of Li metal. However, the three-electrode cell with a reference electrode (saturated calomel electrode, SCE for this work) can provide a stable reference voltage for studying the electrochemical behavior of the working electrode (LMO for this work). Therefore, we perform electrochemical tests for LMO in aqueous electrolytes using the three-electrode cell. We first tested the charge/discharge properties of LMO in an aqueous electrolyte (three-electrode cell, 30 mL 1 M Li_2SO_4) and an organic electrolyte (coin cell, 0.05 mL 1 M $LiPF_6$ in EC:DMC = 1:1) at the same specific current of 0.5 A g^{-1}. According to the standard electrode potentials of SCE (0.245 V vs. SHE) and Li metal (−3.042 V vs. SHE), we converted the charge/discharge potential ranges of LMO in the aqueous electrolyte and the organic electrolyte to 0−1.1 V (vs. SCE) and 3.2−4.3 V (vs. Li/Li$^+$), respectively, to ensure that the potential range of LMO in the two electrolytes is consistent and that the theoretical capacity can be maximized. The charge/discharge curves of LMO (Supplementary Fig. 4a, b) indicate that the LMO electrodes exhibit similar specific capacities and voltage plateaus in both aqueous electrolyte and organic electrolyte at the initial cycle. The initial specific capacities of LMO in an aqueous electrolyte and an organic electrolyte are 122.3 mAh g^{-1} and 118.25 mAh g^{-1}, and the coulombic efficiencies are 94.5% and 84.3%, respectively (Supplementary Fig. 5 and Fig. 1a). The coulombic efficiency of an electrode is the percentage obtained by dividing the discharge capacity by the charge capacity. For an electrode without side reactions, the coulombic efficiency is theoretically 100%, indicating that the electrochemical reaction is completely reversible. The coulombic efficiency of LMO cycled in the aqueous electrolyte is lower than that of in organic electrolyte (Fig. 1a), indicating that more serious side reations occur in LMO cycling in 1 M Li_2SO_4 solution. During the subsequent cycles, the capacity retention of LMO in aqueous electrolyte is successively preferable and worse compared with organic electrolyte. As shown in Fig. 1a, in region 1 (1−140 cycles), the capacity retention of LMO in aqueous electrolyte (88.4%) is higher than that in organic electrolyte (79.6%). In Region 2 (140−300 cycles), the LMO electrode shows a quick capacity drop in aqueous electrolyte with a capacity retention 61.6% after 300 cycles. The coulombic efficiency of LMO (Supplementary Fig. 5 and Fig. 1a) also begins to decrease in Region 2, indicating that the (de)intercalation of Li^+ ions in LMO electrode becomes irreversible. To identify the precise charge storage mechanism of LMO in aqueous electrolyte, in situ electrochemical quartz crystal microbalance (EQCM) measurements were performed to monitor the mass variation of LMO during cycling in aqueous electrolyte. Generally, Mn dissolution induced by disproportionation reaction of Mn^{3+} in a proton environment will decrease the mass of LMO[25,26]. However, as shown in Fig. 1b and Supplementary Fig. 6, the mass of LMO gradually increases associated with cycling. It should be noted that the electrode tested by EQCM is spray-coated with LMO and does not contain a conductive agent and binder. Therefore, the increase or decrease in electrode mass is the mass change of LMO particles. We found that there is a corresponding relationship between the mass change of LMO and the cycle
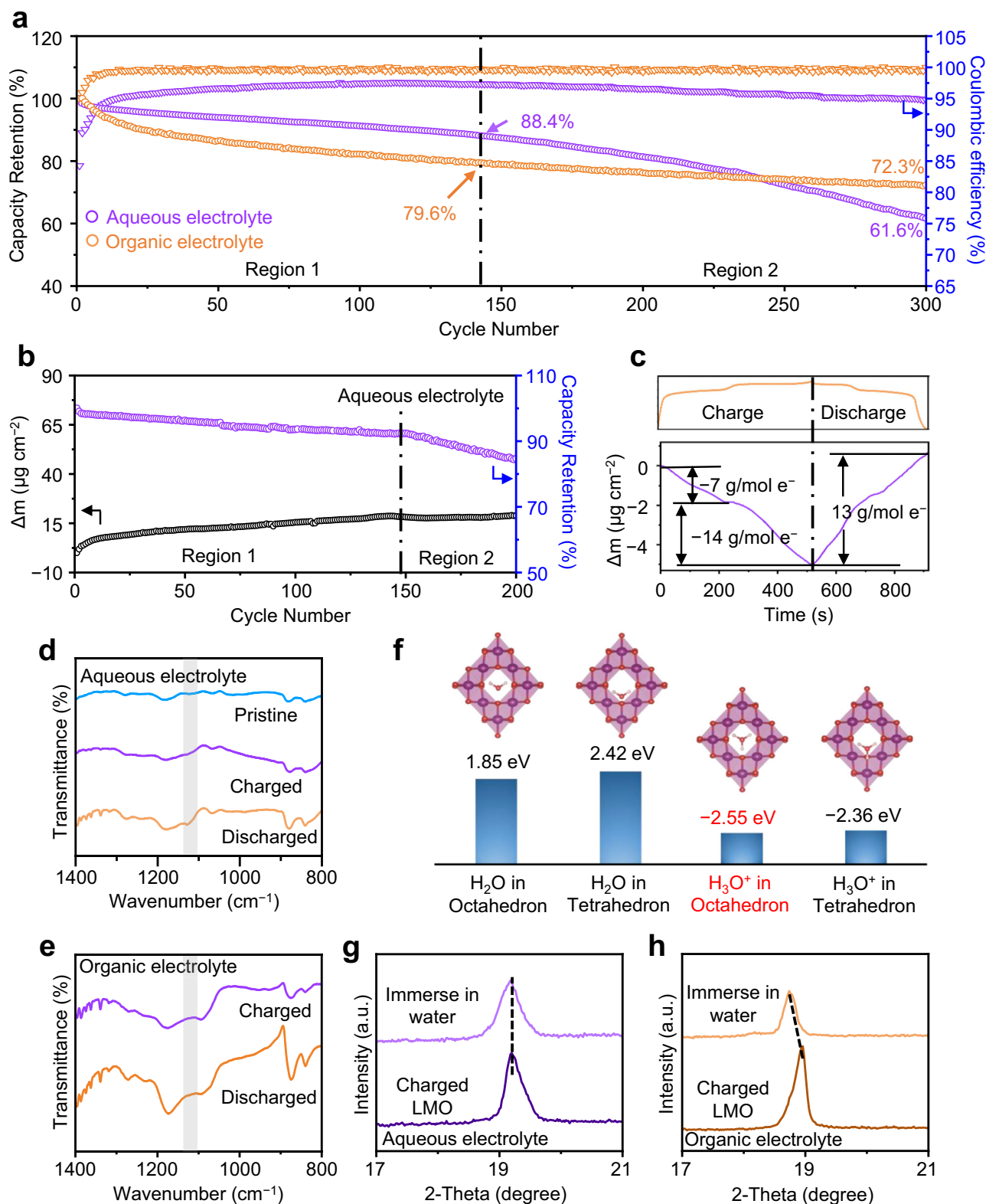
Fig. 1 | The electrochemical analyses, spectral characterizations and theoretical calculations of the phenomenon of H_3O^+ intercalated into $LiMn_2O_4$ lattice. In this figure, all the electrochemical performances of $LiMn_2O_4$ (LMO) electrodes in aqueous electrolyte were tested in a three-electrode cell with 30 mL 1 M Li_2SO_4 and that of in organic electrolyte were tested in a CR2032 coin cell with 0.05 mL 1 M $LiPF_6$ in EC:DMC = 1:1. **a** Cycle performance of LMO in aqueous electrolyte and in organic electrolyte at a specific current of 0.5 A g^{-1} (The initial capacity of LMO electrode in organic electrolyte and aqueous electrolyte are 122.3 mAh g^{-1} and 118.25 mAh g^{-1}, respectively). **b** The EQCM testing (black curve) of LMO electrode during cycling in 30 mL 1 M Li_2SO_4 (violet curve). **c** Analyses of mass changes of LMO during a single charge/discharge curve. The FTIR spectra of LMO at different stages of the charge/discharge progress in (**d**) aqueous electrolyte and (**e**) organic electrolyte. **f** The formation energy of LMO with H_2O/H_3O^+ in various cation sites. The XRD spectra of LMO charged in (**g**) aqueous electrolyte and (**h**) organic electrolyte and after immersion in water for 12 h.

performance. When the mass increase rate of LMO slows down, the cycle performance also starts to degrade rapidly. The EQCM curves (bottom) and corresponding charge/discharge curves (top) of LMO are shown in Fig. 1c, and the mass variation analyses are shown in Supplementary Fig. 7. During the beginning of the charge process, the LMO exhibits mass loss with $\Delta m/dq$ of -7 g mol^{-1} which can be attributed to Li deintercalation in LMO lattice, and the mass loss with $\Delta m/dq$ of -14 g mol^{-1} at the high voltage of charge progress can be attributed to Li$^+$ deintercalation together with Mn dissolution. During the discharge process, the mass gain $\Delta m/dq$ is 13 g mol^{-1}, which exceeds the mass of Li$^+$ intercalation. We consider that the asymmetrical mass change of LMO between charge and discharge in aqueous electrolyte may be attributed to H$_2$O or H$_3$O$^+$ intercalation together with Li$^+$, and the content of crystal H$_2$O or H$_3$O$^+$ tends to be saturated associated with the cycling. The Tourier transform infrared spectroscopy (FTIR) spectra of LMO cycled in aqueous electrolyte (Fig. 1d) show a new peak at 1120 cm^{-1}, which is absent in the FTIR spectra of LMO cycled in organic electrolyte (Fig. 1e). This peak may be attributed to the $-$OH signal caused by crystal H$_2$O (or H$_3$O$^+$) in LMO lattice[27]. The O 1s X-ray photoelectron spectroscopy (XPS) was performed to study the lattice $-$OH content in LMO surface after different cycles. As shown in Supplementary Fig. 8, LMO surface has a high lattice $-$OH content (30.02%) after 100 cycles. Moreover, with the further cycling of the LMO electrode, the signal of lattice $-$OH still increases slowly (35.16% for 200 cycles and 42.48% for 300 cycles). The result shows that the lattice $-$OH content in LMO surface increases and tends to slow down with the cycling. To determine the intercalated species and their precise sites in LMO lattice, the formation energies (E^F) of LMO with H$_2$O or H$_3$O$^+$ in tetrahedral sites and octahedral sites are calculated by density functional theory (DFT) based on the following expression:

$$E^F = E^F_{\text{Total}} - \mu_{\text{LMO}} - \mu_{\text{H}_2\text{O}/\text{H}_3\text{O}^+} \qquad (1)$$

where E^F_{Total} is the total energy of the LMO with H$_2$O or H$_3$O$^+$; μ_{LMO} and $\mu_{\text{H}_2\text{O}/\text{H}_3\text{O}^+}$ are the chemical potentials of LMO and H$_2$O or H$_3$O$^+$, respectively. For most molecular, chemical potentials are equal to the DFT total energies of their ground states.

The calculation models are placed in Supplementary Fig. 9 and the DFT calculation results are shown in Fig. 1f. The E^F of H$_2$O in tetrahedral sites and octahedral sites are $+1.85$ eV and $+2.42$ eV, respectively, which indicates that the H$_2$O is thermodynamically unfavorable in both tetrahedral sites and octahedral sites. However, the E^F of H$_3$O$^+$ in tetrahedral sites and octahedral sites are -2.55 eV and -2.36 eV, respectively, suggesting that H$_3$O$^+$ is thermodynamically favorable in LMO lattice and H$_3$O$^+$ may spontaneously intercalate when Li site vacancies are formed. We immerse the LMO electrodes (fully charged in aqueous and organic electrolytes, respectively) in ultra-pure water for 12 h and perform XRD on them. Figure 1g, h show that the (111) peak of LMO cycled in organic electrolyte significantly shifted to a lower angle after immersion in ultra-pure water. As predicted, the spontaneous insertion of H$_3$O$^+$ causes the expansion of the LMO lattice, resulting in a shift of (111) peak. We monitor the dynamic pH value change of 1 M Li$_2$SO$_4$ during charge/discharge process by using a pH meter. The results are shown in Supplementary Fig. 10, with the pH of the pristine electrolyte is 7.59. In the initial cycles, the electrolyte pH value is 7.66 in the charging state, and the value changes to 7.72 in the discharging state. The observed increase in pH value may be attributed to the insertion of H$_3$O$^+$. After certain cycles, the electrolyte pH values maintain 7.68 and 7.72 during charging state and discharging state, respectively. According to the above studies, we confirm that the intercalation of H$_3$O$^+$ into cation vacancies of LMO lattice will occur during charge/discharge processes in aqueous electrolyte. However, the role of H$_3$O$^+$ in the stability of LMO structure and the rapid capacity drop of LMO when the H$_3$O$^+$ is saturated in LMO require further exploration. We will further address these issues in subsequent chapters.

Crystal H$_3$O$^+$ enhances the structural stability of LMO

To investigate the effects of crystal H$_3$O$^+$ on the structure stability of LMO, we perform XRD on the fully charged LMO in aqueous electrolyte and organic electrolyte before and after immersion in ultra-pure water. The LMO containing crystal H$_3$O$^+$ exhibits superior structural stability, as the overall XRD spectrum in Supplementary Fig. 11a does not change before and after immersion in ultra-pure water. Supplementary Fig. 11b shows that the XRD spectrum of LMO electrode charged in organic electrolyte generated additional peaks after immersion in ultra-pure water, indicating that the LMO without crystal H$_3$O$^+$ undergoes structural degradation due to proton electrophilic attack. To understand the effect of crystal H$_3$O$^+$ on the structure evolution of LMO during the charge/discharge process, the Mn 2p XPS spectra of LMO cycled in aqueous electrolyte after different cycles are shown in Fig. 2a. It can be concluded that the ratio of Mn^{4+} on LMO surface increases with cycling. It can be seen in Supplementary Fig. 12, that in LMO, Li-ions occupy the tetrahedral sites. When crystal H$_3$O$^+$ occupies one octahedral site, the nearby two Li-ions will be subject to repulsive force and are not suitable to occupy the tetrahedral sites, because the H$_3$O$^+$-occupied octahedral site and the two LiO$_4$ tetrahedral sites are face-sharing. With the reduction of Li$^+$ content, to maintain charge balance, the surrounding Mn^{3+} increases to Mn^{4+}. The Jahn-Taller (J-T) inactive Mn^{4+} can suppress the cooperative J-T effect and avoid the Mn dissolution. Electron energy loss spectroscopy (EELS) spectra of Mn $L_{3,2}$-edge and O K-edge are performed from surface to subsurface regions for LMO cycled in aqueous electrolyte. The high-angle annular dark-field scanning transmission electron microscopy (HAADF-STEM) image with EELS line-scan path is shown in Fig. 2b and the EELS spectra are presented in Fig. 2c. In O-K edge spectra, there are three main peaks which are labeled as A$_1$, A$_2$, and A$_3$. Those peaks correspond to transition of electrons from O 1s to the hybridized bands of O 2p and Mn 3d. The increase in the intensity ratio of the A$_1$ peak to A$_3$ peak, from the surface to the interior phase, indicates a reduction in the Mn valence state of the MnO$_6$[28]. The A$_2$ peak may correspond to the inserted H$_3$O$^+$ in the surface lattice. The O-K edge indicates the H$_3$O$^+$ concentration gradient distribution and the reduction of Mn valence from surface to subsurface of LMO. The peaks of Mn-L_3 and Mn-L_2 exhibit chemical shifts to higher energy loss and a higher intensity ratio of L_2/L_3, fully demonstrating the increase of Mn valence states on the surface of LMO[28]. The etching XPS is also used to analyze the H$_3$O$^+$ content distribution from the surface to the interior phase of the cycled LMO. As shown in Supplementary Fig. 13, the lattice $-$OH signal decreases from surface to interior phase of LMO, indicating the gradient distribution of H$_3$O$^+$ on the LMO surface. The above analyses of LMO surface and subsurface through XPS and HAADF-STEM with EELS measurements demonstrate the formation of a gradient Mn^{4+}-rich protective shell by crystal H$_3$O$^+$ (Fig. 2d). Since Mn^{4+} is J-T inert, this protective shell may protect the spinel structure of LMO from H$^+$ attack during cycling in aqueous electrolyte.

The high resolution transmission electron microscope (HRTEM) image and corresponding Fast Fourier Transform (FFT) analysis of the pristine LMO are provided in Supplementary Fig. 14. The as-prepared LMO shows a highly crystallized spinel structure with continuous lattice fringes. After 50 cycles in organic electrolyte, the LMO shows amorphous regions and distorted lattice fringes (Fig. 2e), indicating severe structural degradation. The corresponding FFT pattern (Fig. 2f) shows that the spots in red circles can be indexed to the spinel LMO and the extra spots in yellow circles can be indexed to the Li-rich Li$_2$MnO$_3$. The attack of proton leads to Mn dissolution and further triggers the migration of the Mn in LMO[29]. This dissolution and migration lead to the generation of Li-rich Li$_2$MnO$_3$. While in aqueous electrolyte (Fig. 2h), the cycled LMO maintains the well-resolved spinel structure. The FFT pattern (Fig. 2i) further confirms the spinel LMO without an extra phase. Even after 200 cycles in aqueous electrolyte, the HRTEM image and FFT analysis of LMO (Supplementary Fig. 15a, b) still display intact cubic spinel phase, suggesting that the spinel

structure is well preserved in aqueous electrolyte. The XRD spectra presented in Supplementary Fig. 16 additionally demonstrate that LMO will undergo structural degradation in organic electrolyte during charge/discharge processes, while its structural stability is higher in aqueous electrolyte. We carefully performed in situ XRD coupled with charge/discharge process on LMO in the organic electrolyte and the
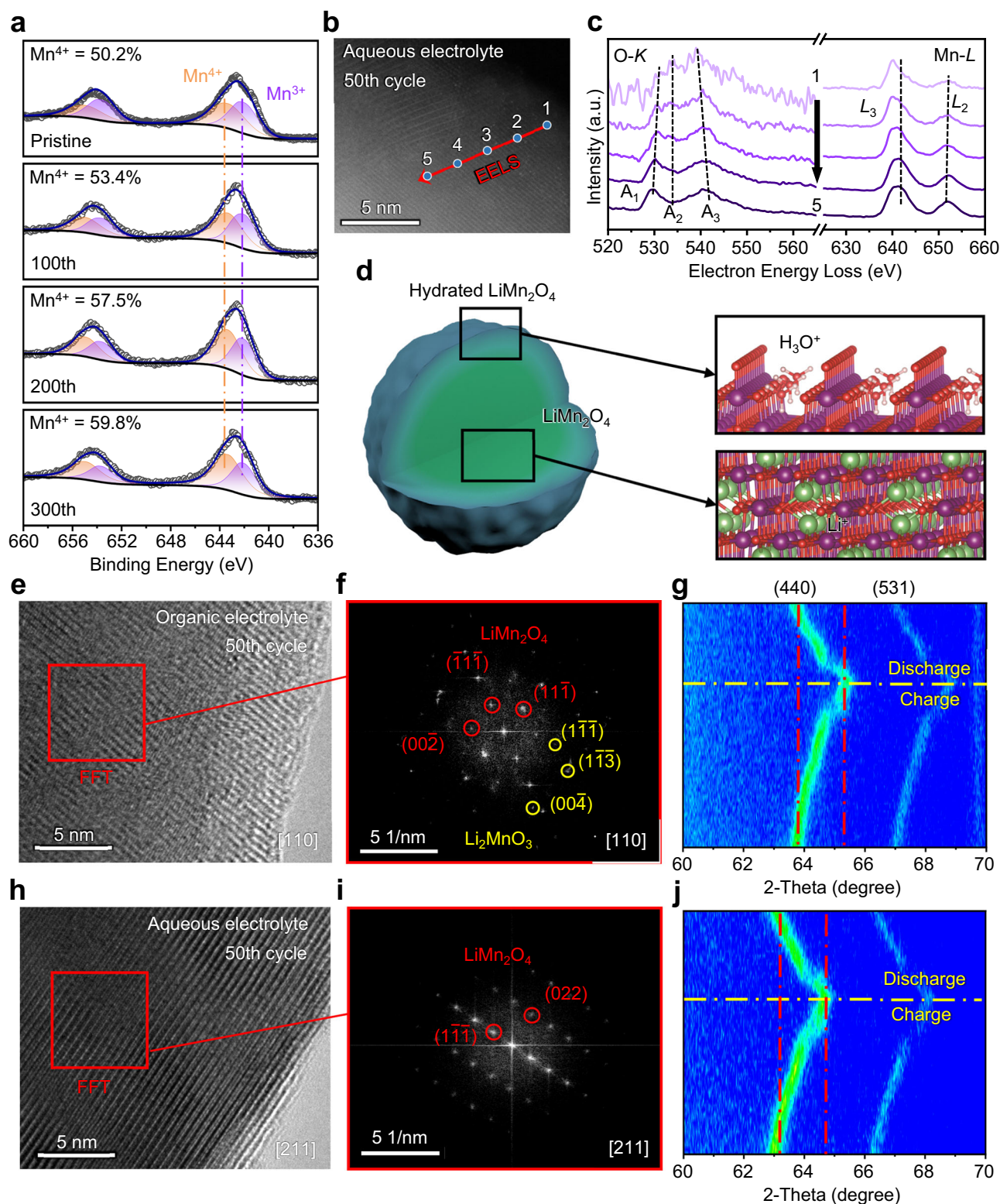

Fig. 2 | The structural evolution of the LMO in different electrolytes. a The Mn $2p$ XPS spectra of LMO after different cycles. **b** HAADF-STEM images with EELS line-scan path of LMO. **c** Selected EELS O K-edge and Mn $L_{3,2}$-edge spectra at different depths of LMO after cycling in aqueous electrolyte. **d** Scheme of the surface structure of LMO after a certain number of cycles. **e** HRTEM image and (**f**) FFT analysis of LMO cycled in organic electrolyte. **g** Partial in situ XRD pattern of LMO during the first charge/discharge in organic electrolyte. **h** HRTEM image and (**i**) FFT analysis of the LMO cycled in aqueous electrolyte. **j** Partial in situ XRD pattern of the LMO during the first charge/discharge in aqueous electrolyte. The in situ XRD measurements of LMO electrodes in aqueous electrolyte were tested in a XRD-WB cell with 0.05 mL 1 M Li_2SO_4 and that of in organic electrolyte were tested in a XRD-LIB cell with 0.05 mL 1 M $LiPF_6$ in EC:DMC = 1:1.

aqueous electrolyte, respectively. The organic in situ XRD cell (LIB-XRD) structure and aqueous in situ XRD cell (WB-XRD) structure are shown in supplementary Fig. 17a, b, respectively. The electrode parameters, electrolyte dosage, specific current, and other details of the in situ cells are in the methods. The in situ XRD full spectra (Supplementary Figs. 18–20) indicate that the structural evolution of LMO during charge/discharge in organic electrolyte and aqueous electrolyte is similar. To further study the subtle differences in the structural evolution of LMO in different electrolytes, the partial in situ XRD results are enlarged in Fig. 2g. The selected peak at approximately 63° is assigned to the (440) peak of LMO, which is free from the hindrance of the substrate. The (440) peak shifts to a high/low angle, which correlates with the electrochemical (de)intercalation of Li^+. The (440) peak shifts smoothly in the low voltage region and splits in the high voltage region, confirming that LMO undergoes a monophasic solid solution reaction at high Li content and a biphasic reaction at low Li content[30,31]. A significant difference in Mn−O bond lengths between undistorted octahedra and J-T distorted octahedra contributed to the abrupt variation in lattice parameters. Figure 2j shows that the phase transition of LMO in aqueous electrolyte is similar to that in organic electrolyte. Notably, the biphasic transition in the high voltage region is suppressed and even disappears after further cycling (partial in situ XRD pattern of LMO after 200 cycles in Supplementary Fig. 21). The suppression of cooperative J-T effect mitigates the elongation of the Mn−O bonds, leading to a slight variation in lattice parameter. The calculated a lattice parameter change in Supplementary Fig. 22 further demonstrates that the lattice variation of LMO is suppressed during charge/discharge in aqueous electrolyte[32]. In addition, consistent with existing reports, the strong hydrogen bond between crystal H_2O and lattice H could effectively mitigate the H attack on lattice O, thereby alleviating the migration and dissolution of transition metals[24].

Crystal H_3O^+ leads to sluggish Li^+ diffusion kinetics

As mentioned above, crystal H_3O^+ effectively improves the structural stability of LMO, but the cycle performance of LMO in aqueous electrolyte is still unsatisfactory. As shown in Fig. 1a, b, although the cycle performance of LMO in aqueous electrolyte is higher than that in organic electrolyte in the early stage, as the cycle number increases, its capacity retention decreases significantly. To reveal the culprit of sudden capacity drops in Region 2 (Fig. 1a), the electrochemical characteristics of LMO were further investigated. Figure 3a, d provide the corresponding charge/discharge curves. It can be seen that similar charge/discharge processes are exhibited upon initial cycles, with two typical charge/discharge plateaus of LMO observed at 4.05 and 4.15 V (vs. Li^+/Li) in organic and aqueous electrolytes. During cycling in organic electrolyte, the capacity of LMO gradually decreases and the two typical charge/discharge plateaus are maintained. While in aqueous electrolyte, the two typical plateaus of charge/discharge curves are weakened and the voltage hysteresis is aggravated during cycling. Supplementary Figs. 23, 24 provide the dQ/dV analyses to compare the voltage variation of LMO in the two electrolytes. The enlarged areas of dQ/dV in Fig. 3b−e show that, in aqueous electrolyte, the peaks corresponding to the two plateaus transform into bulges. These results suggest that the LMO suffers from severe electrode polarization and dramatic electrochemical kinetic deterioration in aqueous electrolyte. The rate performance of the pristine LMO and after 200 cycles in the two electrolytes are provided in Fig. 3c, f. The cycled LMO electrode in organic electrolyte exhibits slightly lower capacity but comparable rate performance to the pristine one (Fig. 3c). In comparison, in aqueous electrolyte, the pristine LMO shows a better rate performance due to the high Li^+ conductivity of its electrolyte (Fig. 3f). It is noteworthy that although the capacity of LMO dropped significantly after 200 cycles in aqueous electrolyte at a specific current of 0.5 A g^{-1} (from 106.67 mAh g^{-1} to 78.7 mAh g^{-1}), it recovered to a high specific capacity

of 105.04 mAh g^{-1} at a low specific current of 0.1 A g^{-1} (Fig. 3f). The poor rate capability of the electrode indicates that the Li^+ diffusion of LMO is challenged after cycling in aqueous electrolyte. The crystal H_3O^+ is usually firmly anchored in the lattice due to hydrogen bonds and its molecular size, which may block the tetrahedron-octahedron-tetrahedron diffusion pathway of Li^+[10]. We further verified the adverse effect of crystal H_3O^+ on Li diffusion by removing crystal H_3O^+. The LMO cycled after 300 cycles in aqueous electrolyte was heated to 150 °C for 12 h to remove the crystal H_3O^+. The charge/discharge curves of the cycled LMO before and after heat treatment are shown in Fig. 3g, h. Unlike the cycled LMO with low capacity (33.2 mAh g^{-1}) and severe voltage hysteresis, the LMO after removing crystal H_3O^+ shows redux capacity (107.4 mAh g^{-1}) and reduced polarization. However, the removal of the H_3O^+ usually accompanies the loss of lattice O, and the stability of LMO is significantly compromised, resulting in a rapid capacity drop in subsequent cycles (Fig. 3g). Therefore, more effective strategies should be implemented to address the unlimited insertion of the H_3O^+. These electrochemical analyses demonstrate that the capacity drop of the LMO in aqueous electrolyte is mainly dominated by the sluggish Li^+ diffusion kinetics. Although crystal H_3O^+ in the LMO surface lattice can enhance structural stability, its excessive occupation in the interstitial sites hinders the Li^+ diffusion, resulting in a rapid capacity decline of LMO. Regulating the H_3O^+ concentration in LMO in aqueous electrolytes is of paramount importance for enhancing LMO performance.

Improving the cycle performance of LMO by regulating the hydrogen bond networks of aqueous electrolyte

It has been reported that the addition of solvents that form hydrogen bonds with H_2O can decrease the number of H_2O in the Li^+ solvation shell, thereby broadening the electrochemical stability window of aqueous electrolyte[33,34]. Whether the reduction of H_2O population at electrode/electrolyte interface plays a role in the control of crystal H_3O^+ content in LMO? For verification, we added different content of acetonitrile (ACN) to 1 M Li_2SO_4, since ACN can accumulate on the electrode surface and form hydrogen bond interactions with H_2O[35,36]. Fig. 4a displays the FTIR spectra of 1 M Li_2SO_4 with different content of ACN and the pure ACN. The peak at 2253 cm^{-1} can be attributed to C ≡ N stretching vibration. The peak is blue-shifted when added to 1 M Li_2SO_4 electrolyte, indicating the formation of the hydrogen bonds between ACN and H_2O. The Raman spectra of 1 M Li_2SO_4 with different content of ACN and the pure ACN are shown in Fig. 4b, the peaks at ~3250 cm^{-1} and ~3412 cm^{-1} are assigned to the asymmetric/symmetric O−H stretching vibration from hydrogen bonds, respectively, and the peak at ~3612 cm^{-1} corresponds to free O−H in H_2O molecules. With the addition of the ACN, the free H_2O molecules and the asymmetric/symmetric O−H stretching vibration ratio are reduced. The Raman spectra reveal that more water molecules are included in the hydrogen network, and the hydrogen network is regulated due to the addition of ACN. The linear sweep voltammetry (LSV) curves of 30 mL 1 M Li_2SO_4 with different content of ACN are tested in a three-electrode cell. Supplementary Fig. 25 shows that the electrochemical windows are gradually broadened with the concentration of ACN. These results indicate that the addition of ACN could regulate the hydrogen network and weaken the activity of H_2O. According to XPS spectra of N 1s and C 1s in Supplementary Figs. 26, 27, the addition of ACN decomposes on the electrode surface and covers the LMO surface, which may further weaken the activity of H_2O on the LMO surface. The O 1s XPS spectra (Supplementary Fig. 28) are applied to detect the crystal H_3O^+ in cycled LMO and the qualitative crystal H_3O^+ content is shown in Fig. 4c. By using ACN as an additive, the lattice −OH content in cycled LMO (after 100 cycles) decreased with increasing ACN content. The electrochemical impedance spectroscopy (EIS) spectra of LMO in 1 M Li_2SO_4 with different content of ACN are shown in Supplementary Fig. 29. With the
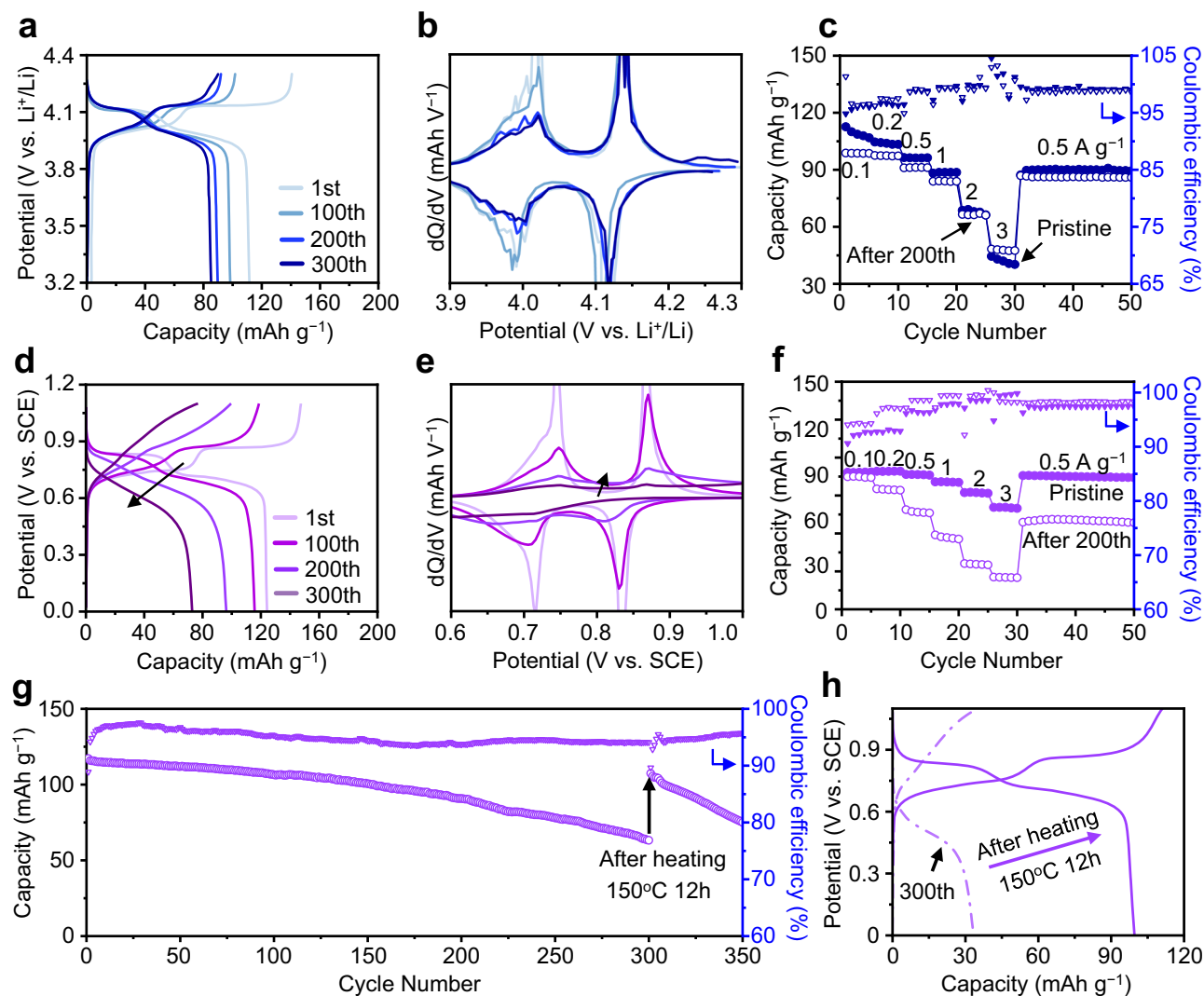
Fig. 3 | Electrochemical performance analysis of the LMO in different electrolyte. In this figure, all the electrochemical performances of LMO electrodes in aqueous electrolyte were tested in a three-electrode cell with 30 mL 1 M Li_2SO_4 and that of in organic electrolyte were tested in a CR2032 coin cell with 0.05 mL 1 M $LiPF_6$ in EC:DMC = 1:1. **a** Charge/discharge curves and (**b**) dQ/dV analysis of LMO in organic electrolyte at a specific current of 0.5 A g^{-1}. **c** The rate capability of pristine LMO and cycled LMO in organic electrolyte. **d** Charge/discharge curves and (**e**) dQ/dV analysis of LMO in aqueous electrolyte at a specific current of 0.5 A g^{-1}. **f** The rate capability of pristine LMO and cycled LMO in aqueous electrolyte. **g** The cycle performance and (**h**) the charge/discharge curves of the LMO at a specific current of 0.5 A g^{-1} before and after heating at 150 °C.

excessive insertion of H_3O^+, H_3O^+ will block the diffusion channel of Li$^+$ and increase the charge transfer resistance on LMO surface. With the addition of ACN, the charge transfer resistance of LMO surface is greatly reduced. The galvanostatic intermittent titration technique (GITT) measurements in Supplementary Fig. 30 also show that LMO exhibits ion diffusion efficiencies of ~4.51 × 10^{-10} cm^2 S^{-1}, -1.44 × 10^{-9} cm^2 S^{-1}, and -1.23 × 10^{-9} cm^2 S^{-1} for LMO cycled 1 M Li_2SO_4 with 0%, 10%, and 50% ACN additive, respectively. These results indicate that ACN inhibits the excessive insertion of H_3O^+, reduces the blocking of the Li$^+$ diffusion channels, and effectively improves the charge transfer on the LMO surface. The cycle performances of LMO in different electrolytes (1 M Li_2SO_4 with 0%, 10%, 50% ACN and 1 M $LiPF_6$ in EC:DMC = 1:1) are shown in Fig. 4d. The LMO exhibits significantly improved cycle performance in 30 mL 1 M Li_2SO_4 with 50% ACN compared with 1 M $LiPF_6$ in EC:DMC = 1:1 and 30 mL 1 M Li_2SO_4 with 0% and 10% ACN. In addition, the coulombic efficiency of LMO electrode increases from ~95% (1 M Li_2SO_4) to ~99% (1 M Li_2SO_4 with 50% ACN). We further investigate the long-term cycle stability of LMO electrode in 1 M Li_2SO_4 with 0% and 50% ACN. As shown in Fig. 4e, after 10,000 cycles, LMO shows a capacity retention of 82.1%

with a coulombic efficiency of 99.5% in 1 M Li_2SO_4 with 50% ACN. The related charge/discharge curves show that LMO cycled in 1 M Li_2SO_4 with 50% ACN (Supplementary Fig. 31) exhibits a reduced polarization and a superior capacity retention than that of LMO cycled in 1 M Li_2SO_4 (Supplementary Fig. 32). These results indicate that an appropriate amount of crystal H_3O^+ can not only stabilize the LMO lattice but also avoid the slow Li$^+$ diffusion kinetics, thus making the cycling performance of LMO in aqueous electrolytes higher than that in organic electrolytes. The rate performance of the LMO in different electrolytes after 200 cycles is shown in Fig. 4f, which once again proves that the crystal H_3O^+ content directly affects the diffusion of Li$^+$. Figure 4g illustrates that in organic electrolyte, LMO undergoes structural degradation and capacity fading due to side reactions at the electrode/electrolyte interface. In aqueous electrolyte, crystal H_3O^+ can enhance the structural stability of LMO benefit from the formation of a gradient Mn^{4+}-rich protective shell. However, excess crystal H_3O^+ will lead to severe polarization caused by poor Li$^+$ diffusion kinetics. With the addition of ACN, the hydrogen network of aqueous electrolyte is regulated, and ACN may decompose on the electrode surface, thereby weakening the reactivity of H_2O molecules
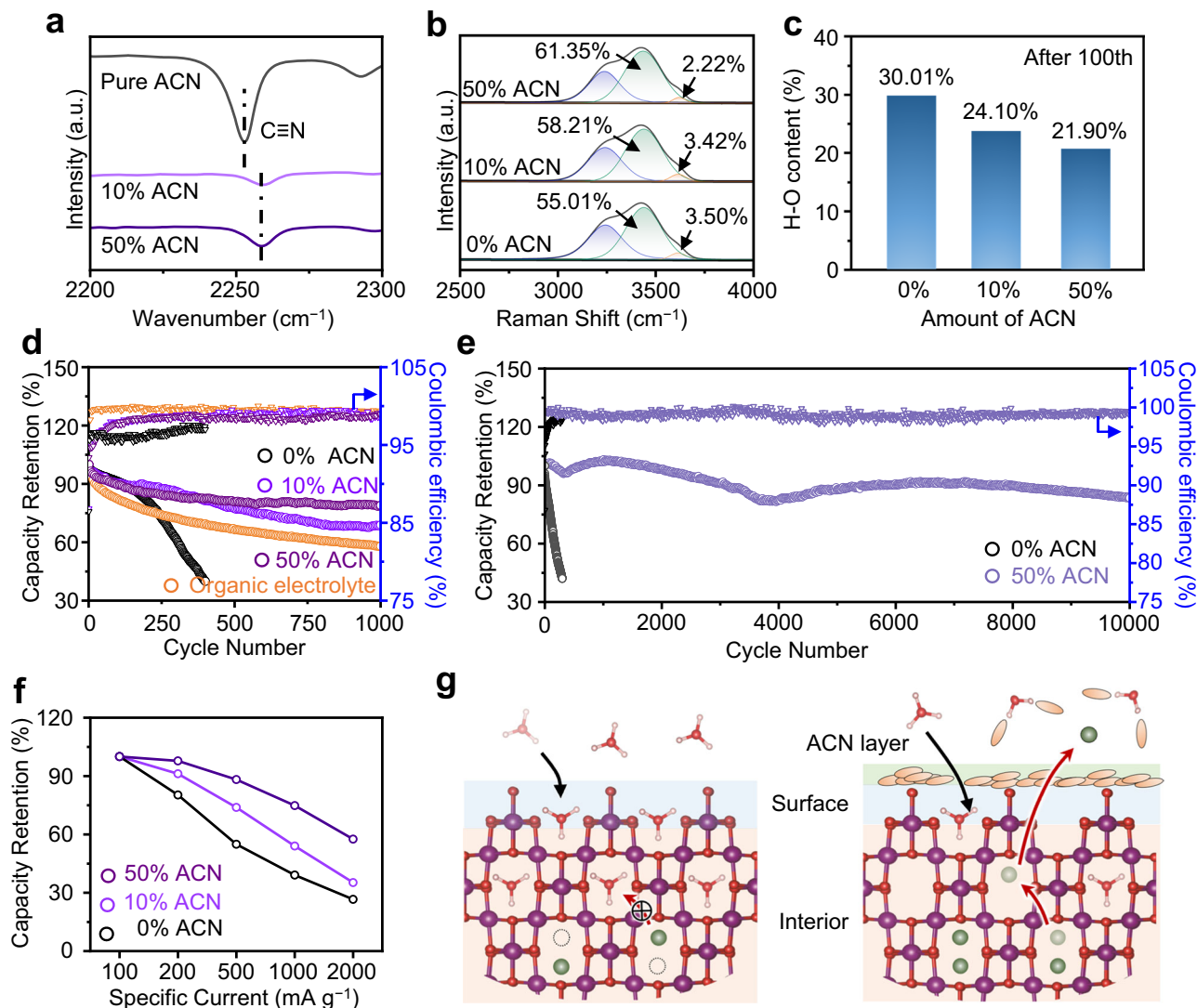
Fig. 4 | The characteristic and electrochemical performance of the LMO in aqueous electrolyte with Acetonitrile additive. In this figure, all the electrochemical performances of LMO electrodes in aqueous electrolyte were tested in a three-electrode cell and that of in organic electrolyte were tested in a CR2032 coin cell. **a** The FTIR spectra of pure Acetonitrile (ACN) and 1 M Li_2SO_4 with different content of ACN. **b** The Raman spectra of 1 M Li_2SO_4 with different content of ACN. **c** O–H contents on LMO surface after cycling in 1 M Li_2SO_4 with different content of ACN for 100 cycles. **d** Cycle performances of LMO in 0.05 mL 1 M $LiPF_6$ in EC:DMC = 1:1 and 30 mL 1 M Li_2SO_4 with different content of ACN at a specific current of 0.5 A g^{-1} for 1000 cycles. **e** Cycle performance of LMO in 30 mL 1 M Li_2SO_4 with 0% and 50% ACN at a specific current of 5 A g^{-1} for 10,000 cycles. **f** The rate capability of LMO in 30 mL 1 M Li_2SO_4 with different content of ACN after 200th cycles. **g** Schematic illustration of crystal H_3O^+ occupancy and its effect on Li^+ diffusion in LMO.

and achieving a long-term stable cycle of LMO with optimized content of the crystal H_3O^+.

Discussion

In summary, we demonstrate the thermodynamically spontaneous insertion of the H_3O^+ into LMO when cycled in aqueous electrolyte. According to electrochemical analyses and structural characterizations, we propose that the interaction between H_3O^+ and LMO leads to a more robust lattice structure but a poor Li^+ diffusion ability. Through surface crystal H_3O^+, a gradient Mn^{4+}-rich protective shell is formed to improve proton tolerance and suppress lattice distortion of LMO during charge/discharge process. Thus, the structural degradation is relieved and the cycle stability of LMO is improved. However, the further insertion of the H_3O^+ blocks the Li^+ diffusion pathway and forms a poor conductive surface which leads to the rapid capacity fading. By regulating the solvation structure, the insertion of the H_3O^+ is limited, effectively improving the cycle stability of the LMO in aqueous electrolyte. The present work reveals the neglected interaction between aqueous electrolyte and LMO and demonstrates the capacity fading mechanism of the LMO cycled in aqueous electrolyte. Providing insights into the LMO electrode which is cycled in aqueous electrolyte will facilitate the design of high energy density and long cycle life ALIBs.

Methods

Materials synthesis

The ethanol (AR, 99.7%), acetonitrile (ACN, AR, 99%), 1-Methyl-2-pyrrolidinone (NMP, AR, 99%), Li_2SO_4 (99.9%), CH_3COOLi (99%) and $(CH_3COO)_2Mn$ (98%) were purchased from Aladdin Reagent Co. Ltd., China. The polyvinylidene fluoride (PVDF) was purchased from Arkema (China) Investment Co. Ltd., China. The ultra-pure water was produced by laboratory water purification system (TE-S20, Hitech Instruments Co. Ltd., China) with a resistance of 18.2 MΩ cm. The LMO was prepared by heating a mixture of CH_3COOLi and $(CH_3COO)_2Mn$ (with a Li/Mn ratio of 0.5). 1.02 mg CH_3COOLi was first mixed with 4.92 mg $(CH_3COO)_2Mn$. Then, ethanol was added to the

mixture sample and ground to form a slurry. The slurry was heated at 450 °C in air for 4 h. The gained black sample was grinded up and heated at 700 °C in air for 12 h again. After cooling to room temperature, the product was collected and sealed.

Materials characterization

XRD (MiniFlex600, Cu Kα radiation, Rigaku Co. Ltd.) was applied to investigate the crystal structures of LMO. XPS (ESCALAB250Xi, Thermo Fisher Scientific) and FTIR (NICOLET iS10, ThermoFisher Scientific) were applied to investigate the insertion of H_3O^+ in LMO in aqueous electrolyte. HRTEM (JEOL JEM-2100F, JEOL Ltd.) was used to investigate the structural evolutions of different samples. The beam energy was 200 kV and the resolution was about 1 eV for STEM-EELS measurements.

For the in situ XRD measurements in organic electrolyte, an in situ XRD cell (LIB-XRD, Beijing Science Star Technology Co. Ltd., Supplementary Fig. 16a) with a Be window was used. The LMO electrode (by coating a slurry of 70 wt% LMO, 20 wt% acetylene black, and 10 wt% PVDF in NMP on a smooth surface, dried at 60 °C for 12 h in vacuum, and peeled off) with a diameter of 1.4 cm and Li metal (thickness 0.45 cm) with a diameter of 1.6 cm were used as positive and negative electrode, respectively. A glass fiber film with a diameter of 1.9 cm was used as the separator and a 0.05 mL 1 M $LiPF_6$ in EC:DMC = 1:1 was used as the organic electrolyte.

For the in situ XRD measurements in aqueous electrolyte, an in situ XRD cell (WB-XRD, Beijing Science Star Technology Co. Ltd., Supplementary Fig. 16b) with a Kapton tape window was used. The LMO electrode (by coating a slurry of 70 wt% LMO, 20 wt% acetylene black, and 10 wt% PVDF in NMP on carbon cloth and dried at 60 °C for 12 h) with a diameter of 1.4 cm and active carbon electrode with a diameter of 1.6 cm supported by carbon cloth were used as positive and negative electrode, respectively. A glass fiber film with a diameter of 1.9 cm was used as the separator and 0.05 mL of 1 M Li_2SO_4 solution was used as an aqueous electrolyte.

The galvanostatic charge/discharge processes of LMO electrodes for in situ XRD measurements were tested on an electrochemical workstation (LAND-CT3002A, Wuhan LAND Electronic Co. Ltd.) at a specific current of 0.05 A g^{-1}.

Electrochemical measurements

The prepared LMO was used as the active material. The active material, acetylene black, and PVDF in a 7:2:1 mass ratio were mixed in NMP to form a slurry. The slurry was coated on the current collector and dried in a vacuum at 60 °C for 24 h. The mass loadings of the active materials were kept in the range of 3–4 mg cm^{-2}. The charge/discharge tests and rate performance were carried out by LAND-CT3002A.

We use a CR2032 type coin cell (cell structure is shown in Supplementary Fig. 3b) to test electrochemical performances of LMO in organic electrolyte, where LMO electrode (aluminum foil as the current collector) was the positive electrode and Li metal (thickness of 0.45 cm) was the negative electrode. The positive electrode diameter is 1.4 cm and the negative electrode diameter is 1.6 cm. A glass fiber film with a diameter of 1.9 cm was used as the separator and a 0.05 mL 1 M $LiPF_6$ in EC:DMC = 1:1 was used as the organic electrolyte.

We use a three-electrode cell (cell structure is shown in Supplementary Fig. 3a) to test LMO performance in the aqueous electrolyte, where LMO electrode (1×2 cm^2 carbon cloth as the current collector, and the active material coating area is 1×1 cm^2) is the working electrode, a SCE is the reference electrode, and a Pt plate (1×2 cm^2) is the counter electrode. The three-electrode cell uses 30 mL of 1 M Li_2SO_4 solution containing different amounts of ACN (0%, 10%, and 50%) as the aqueous electrolyte.

The Electrochemical Quartz Crystal Microbalance (QCM200, Stanford Research Systems) measurement was applied to study the mass change of the electrode accompanied by charge/discharge progress. The changed molecular weight of ion (Mw) was calculated by $M_w = \frac{\Delta m\, n\, F}{\Delta Q}$, where F is Faraday constant (96485 C mol^{-1}), n is the valence number of ions, and ΔQ is the charge quantity passed through the electrode in Coulombs.

The Electrochemical Impedance Spectroscopy (EIS) measurement was applied by an electrochemical workstation (VMP3, Biologic) to study the charge transfer resistance of LMO electrode. The EIS measurements are performed with 10 mV perturbation amplitude in the range from 100 kHz to 10 mHz in automatic sweep mode from high to low frequencies.

The GITT curves were performed on LAND-CT3002A in a three-electrode cell with 30 mL 1 M Li_2SO_4 at a specific current of 0.5 A g^{-1}, the constant current was applied for 180 s and rest for 3600 s.

All the above electrochemical tests were performed in thermostatic box with a constant temperature of 25 °C.

DTF calculation method

The first-principles calculations within the framework of DFT were calculated using the Vienna Ab Initio Simulation Package (VASP)[37]. The exchange-functional was treated by Perdew-Burke-Ernzerhof (PBE)[38] functional and the projector augmented wave (PAW) method[39] was applied for structural optimization. The Cut-off energy of the plane-wave basis was set at 600 eV for all calculations. Conjugate gradient energy minimization was used to optimize atom position and lattice parameter until forces converged to 0.005 eVÅ^{-1} and the energy converged to 10^{-5} eV. The effective U value of 3.9 is assigned to Mn^{3+}/Mn^{4+}. A $3 \times 3 \times 3$ Monkhorst Pack k-point grid was applied to sample reciprocal space. All calculations were performed in the spin-polarized, ferromagnetic state.

Data availability

Source data are provided with the paper. All data supporting the finding in the study are presented within the main text and the supplementary information. Source data are provided with this paper.

References

1. Li, W., Dahn, J. R. & Wainwright, D. S. Rechargeable lithium batteries with aqueous electrolytes. *Science* **264**, 1115–1118 (1994).
2. von Wald Cresce, A. & Xu, K. Aqueous lithium-ion batteries. *Carbon Energy* **3**, 721–751 (2021).
3. Liu, J. Addressing the grand challenges in energy storage. *Adv. Funct. Mater.* **23**, 924–928 (2013).
4. Wang, M. et al. A −60 °C low-temperature aqueous lithium ion-bromine battery with high power density enabled by electrolyte design. *Adv. Energy Mater.* **12**, 2200728 (2022).
5. Cresce, A. et al. Gel electrolyte for a 4 V flexible aqueous lithium-ion battery. *J. Power Sour.* **469**, 228378 (2020).
6. Shu, Q., Chen, L., Xia, Y., Gong, X. & Gu, X. Proton-induced dysfunction mechanism of cathodes in an aqueous lithium ion battery. *J. Phys. Chem. C* **117**, 6929–6932 (2013).
7. Bin, D., Wen, Y., Wang, Y. & Xia, Y. The development in aqueous lithium-ion batteries. *J. Energy Chem.* **27**, 1521–1535 (2018).
8. Liu, Y. et al. Cathode design for aqueous rechargeable multivalent ion batteries: challenges and opportunities. *Adv. Funct. Mater.* **31**, 2010445 (2021).
9. Trócoli, R., Morata, A., Erinmwingbovo, C., La Mantia, F. & Tarancon, A. Self-discharge in Li-ion aqueous batteries: A case study on $LiMn_2O_4$. *Electrochim. Acta* **373**, 137847 (2021).
10. Manthiram, A. A reflection on lithium-ion battery cathode chemistry. *Nat. Commun.* **11**, 1550 (2020).
11. Ramanujapuram, A. et al. Degradation and stabilization of lithium cobalt oxide in aqueous electrolytes. *Energy Environ. Sci.* **9**, 1841–1848 (2016).

12. Seki, H., Yoshima, K., Yamashita, Y., Matsuno, S. & Takami, N. Aqueous lithium-ion battery of Li$_4$Ti$_5$O$_{12}$/LiMn$_2$O$_4$ using a lithium-ion conductive solid electrolytes separator. *J. Power Sour.* **482**, 228950 (2021).

13. Radzi, Z. I. et al. Review of spinel LiMn$_2$O$_4$ cathode materials under high cut-off voltage in lithium-ion batteries: Challenges and strategies. *J. Electroanal. Chem.* **920**, 116623 (2022).

14. Thackeray, M. M. & Amine, K. LiMn$_2$O$_4$ spinel and substituted cathodes. *Nat. Energy* **6**, 566–566 (2021).

15. Asl, H. Y. & Manthiram, A. Reining in dissolved transition-metal ions. *Science* **369**, 140–141 (2020).

16. Ben, L. et al. Unusual spinel-to-layered transformation in LiMn$_2$O$_4$ cathode explained by electrochemical and thermal stability investigation. *ACS Appl. Mater. Interfaces* **9**, 35463–35475 (2017).

17. Zhao, J. et al. High electrochemical stability of octahedral LiMn$_2$O$_4$ cathode material in aqueous and organic lithium-ion batteries. *Colloids Surf A: Physicochem. Eng. Aspects* **634**, 127932 (2022).

18. Xu, J. et al. Aqueous electrolyte design for super-stable 2.5 V LiMn$_2$O$_4$||Li$_4$Ti$_5$O$_{12}$ pouch cells. *Nat. Energy* **7**, 186–193 (2022).

19. Tian, L. & Yuan, A. Electrochemical performance of nanostructured spinel LiMn$_2$O$_4$ in different aqueous electrolytes. *J. Power Sour.* **192**, 693–697 (2009).

20. Ramanujapuram, A. et al. Degradation and stabilization of lithium cobalt oxide in aqueous electrolyte. *Energy Environ. Sci.* **9**, 1841–1848 (2016).

21. Ruffo, R., Wessells, C., Huggins, R. A. & Cui, Y. Electrochemical behavior of LiCoO$_2$ as aqueous lithium-ion battery electrodes. *Electrochem. Commun.* **11**, 247–249 (2009).

22. Boyd, S. et al. Effects of interlayer confinement and hydration on capacitive charge storage in birnessite. *Nat. Mater.* **20**, 1689–1694 (2021).

23. Li, Y. F. & Liu, Z. P. Active site revealed for water oxidation on electrochemically induced δ-MnO$_2$: role of spinel-to-layer phase transition. *J. Am. Chem. Soc.* **140**, 1783–1792 (2018).

24. Xue, L. et al. Stabilizing layered structure in aqueous electrolyte via dynamic water intercalation/deintercalation. *Adv. Mater.* **34**, 2108541 (2022).

25. Chung, K. Y., Shu, D. & Kim, K. B. Determination of the potential range responsible for the replacement of surface film on LiMn$_2$O$_4$. *Electrochim. Acta* **49**, 887–898 (2004).

26. Nishizawa, M., Uchiyama, T., Itoh, T., Abe, T. & Uchida, I. Electrochemical quartz crystal microbalance for insertion/extraction of lithium in spinel LiMn$_2$O$_4$ thin films. *Langmuir* **15**, 4949–4951 (1999).

27. Zhao, Q. et al. Boosting the energy density of aqueous batteries via facile grotthuss proton transport. *Angew. Chemie-Int. Edit.* **133**, 4215–4220 (2021).

28. Erichsen, T., Pfeiffer, B., Roddatis, V. & Volkert, C. A. Tracking the diffusion-controlled lithiation reaction of LiMn$_2$O$_4$ by in situ TEM. *ACS Appl. Energy Mater.* **3**, 5405–5414 (2020).

29. Yaghoobnejad Asl, H. & Manthiram, A. Proton-induced disproportionation of Jahn–Teller-active transition-metal ions in oxides due to electronically driven lattice instability. *J. Am. Chem. Soc.* **142**, 21122–21130 (2020).

30. Bianchini, M. et al. Spinel materials for Li-ion batteries: new insights obtained by operando neutron and synchrotron X-ray diffraction. *Acta Crystallogr. Section B: Struct. Sci. Crystal Eng. Mater.* **71**, 688–701 (2015).

31. Xia, Y. & Yoshio, M. An investigation of lithium ion insertion into spinel structure Li-Mn-O compounds. *J. Electrochem. Soc.* **143**, 825 (1996).

32. Larson, A. C. & Dreele, R. B. V. General structure analysis system (GSAS). Los Alamos National Laboratory Report No. LAUR 86–748 (1985).

33. Dong, D., Xie, J., Liang, Z. & Lu, Y. C. Tuning intermolecular interactions of molecular crowding electrolyte for high-performance aqueous batteries. *ACS Energy Lett.* **7**, 123–130 (2021).

34. Liang, T., Hou, R., Dou, Q., Zhang, H. & Yan, X. The applications of water-in-salt electrolytes in electrochemical energy storage devices. *Adv. Funct. Mater.* **31**, 2006749 (2021).

35. Wang, D. et al. Insight on organic molecules in aqueous Zn-ion batteries with an emphasis on the Zn anode regulation. *Adv. Energy Mater.* **12**, 2102707 (2022).

36. Yamada, Y. et al. Unusual stability of acetonitrile-based super-concentrated electrolytes for fast-charging lithium-ion batteries. *J. Am. Chem. Soc.* **136**, 5039–5046 (2014).

37. Hafner, J. Ab-initio simulations of materials using VASP: density-functional theory and beyond. *J. Comput. Chem.* **29**, 2044–2078 (2008).

38. Perdew, J. P., Burke, K. & Ernzerhof, M. Generalized gradient approximation made simple. *Phys. Rev. Lett.* **77**, 3865 (1996).

39. Blöchl, P. E. Projector augmented-wave method. *Phys. Rev. B* **50**, 17953 (1994).

Author contributions

J.H., L.X., and J.Z. conceived the idea, carried out data analysis, and co-wrote the manuscript. J.H. and Y.J. synthesized the samples, did electrochemical measurements, and performed structural characterizations. Y.H. conducted the DFT calculations. P.W. and X.F. helped with data analyses and discussions. All authors analyzed the results and commented on the manuscript.

Competing interests

The authors declare no competing interests.

Additional information

Supplementary information The online version contains supplementary material available at https://doi.org/10.1038/s41467-024-51060-y.

Correspondence and requests for materials should be addressed to Liang Xue or Junwu Zhu.

Peer review information *Nature Communications* thanks Arthur Cresce, and the other, anonymous, reviewers for their contribution to the peer review of this work. A peer review file is available.

Reprints and permissions information is available at http://www.nature.com/reprints